Materials Today 92 (2026) 241–252

Contents lists available at ScienceDirect

Materials Today

journal homepage: www.elsevier.com/locate/mattod

Locking aggregation states in tough hydrogels through protective domain formation

Hao Nan Qiu [a,1], Chuan Wei Zhang [a,1], Lixin Dai [a], Yichen Yan [a], Ping He [a], Ruoyi Ke [a], Xiaobing Zuo [b], Hua Zhou [b,*], Ximin He [a,**]

[a] Department of Materials Science and Engineering, University of California, Los Angeles, CA 90095, USA
[b] X-Ray Science Division, Argonne National Laboratory, Lemont, IL 60439, USA

ARTICLE INFO

Keywords:
Hydrogels
Poly(vinyl alcohol)
Tough
Anti-swelling
Environmental stability
Free radical crosslinking

ABSTRACT

Tough hydrogels based on physical crosslinking have attracted tremendous attention due to their excellent mechanical properties achieved through controlled polymer chain aggregation via various processing methods. However, the reversible nature of these physical interactions leads to severe mechanical degradation in aqueous environments, where water molecules competitively disrupt hydrogen bonds and dissolve aggregated structures, fundamentally limiting their practical applications. Herein, we propose a strategy to construct protective domains around physical crosslinks that effectively stabilize the network while preserving energy dissipation capabilities. Using poly(vinyl alcohol) (PVA) as a model system, we implement this design through sequential dehydration-induced crystallization and homogeneous free-radical crosslinking (FRC). The resulting protective domains—chemically-crosslinked loose aggregates surrounding crystallites—serve dual functions: shielding physical crosslinks from solvent-induced disruption and storing hidden chain length that enhances extensibility during deformation. Compared to unprotected physically crosslinked hydrogels, this strategy achieves 2.4-fold enhancement in elastic modulus, 2.1-fold increase in breaking strain, and 4.8-fold improvement in toughness, while dramatically improving environmental stability–the mechanical strength retention increases from ~ 20 % to > 80 % after aqueous immersion, with volume expansion reduced from typical 20–30 % to less than 5 %. Microstructural characterization confirms the coexistence of protected crystallites and loose aggregates. The hydrogel is successfully employed as an electrolyte to construct zinc-ion batteries that feature superior cycling performance, enabled by the exceptional environmental stability and strong structural endurance of the hydrogel. This strategy proves generalizable to various physically crosslinked systems, offering a universal design principle for creating mechanically robust and environmentally stable hydrogels.

Introduction

Tough hydrogels represent a transformative class of soft materials that combine high water content with remarkable mechanical properties, [1] opening unprecedented opportunities in biomedical engineering, [2,3] soft robotics, [4,5] and flexible electronics [6,7]. Over the past two decades, researchers have developed numerous strategies to enhance the mechanical performance of these water-swollen networks, moving beyond traditional brittle hydrogels toward materials that rival biological tissues. [8,9] The introduction of double-network architectures by Gong and colleagues pioneered the concept of sacrificial bonds for energy dissipation, achieving toughness values exceeding 1,000 J/m^2. [10,11] Subsequently, various toughening mechanisms have been explored, including electrostatic interaction for rapid self-healing capabilities, [12] hydrophobic association for enhanced stretchability, [13] and hierarchical structuring across multiple length scales for amplified energy dissipation [14]. These advances have yielded hydrogels with tensile strengths reaching tens of megapascals, extensibilities exceeding 2,000 %, and fracture energies approaching those of natural rubber, fundamentally changing our perception of what hydrogels can achieve. [15,16].

Among the diverse strategies for engineering tough hydrogels, the

* Corresponding author at: X-Ray Science Division, Argonne National Laboratory, Lemont, IL, 60439, USA.
** Corresponding author at: Department of Materials Science and Engineering, University of California, Los Angeles, CA 90095, USA.
E-mail addresses: hzhou@anl.gov (H. Zhou), ximinhe@ucla.edu (X. He).
[1] These authors contributed equally to this work.

https://doi.org/10.1016/j.mattod.2025.12.005
Received 3 October 2025; Received in revised form 20 November 2025; Accepted 1 December 2025
Available online 10 December 2025

approach of tuning aggregation through fabrication stands out as a particularly effective and adaptable method. [17,18] This methodology leverages the dynamic and reversible nature of noncovalent associations to create materials with broadly tunable properties. Notably, Wu et al. demonstrated that poly(vinyl alcohol) (PVA) hydrogels could achieve a 300-fold tunability in mechanical properties through the Hofmeister effect, where different ions modulate polymer–polymer versus polymer-water interactions to control chain aggregation. [19] Building on this concept, Hua et al. integrated freeze-casting with salting-out treatments to fabricate hydrogels with tendon-like tensile strength (23.5 MPa) by promoting aligned microstructures and crystallinity. [20] More recently, Qiu et al. revealed that by tuning the temperature and hydrophobic interactions during the swelling process, the formation of polyelectrolyte/surfactant complexes and the vitrification of polymer chains can be systematically controlled, achieving Young's modulus increasing from 0.089 to 95.1 MPa. [21] Likewise, by harnessing polymer chain vitrification as a key design principle, Hu et al. elucidated a two-stage microphase separation and vitrification mechanism during solvent exchange, enabling the fabrication of glassy hydrogels with high stiffness and toughness through hydrophobic aggregation and structural arrest. [22] These aggregation-based strategies highlight the versatility of post-gelation in tailoring hydrogel performance, offering access to mechanical properties ranging from soft brain tissue to tough cartilage. [23,24].

However, despite these remarkable achievements, hydrogels based on physical interactions face critical challenges that limit their practical applications. [25] Their reversible nature renders these non-covalent networks inherently sensitive to environmental conditions, with hydrogen bonds being particularly vulnerable in aqueous environments. Water molecules compete with polymer–polymer hydrogen bonding sites, leading to network swelling and dramatic mechanical degradation, often resulting in a loss of over 70 % of the initial strength. [19] This instability extends to ionic environments, where salting-in ions disrupt polymer aggregation, as well as to extreme pH and elevated temperatures, which break interchain hydrogen bonds and disassemble crystallites. For biomedical applications such as load-bearing implants or long-term tissue scaffolds, this environmental sensitivity poses unacceptable risks. [26] Similarly, in electrochemical energy storage devices, hydrogel electrolytes are attractive due to their high ionic conductivity, flexibility, and ability to maintain intimate electrode–electrolyte contact. However, excessive swelling may occur during operation due to its poor environment stability, leading to increased internal resistance, ion leakage, and mechanical degradation of the electrode–electrolyte interface, thereby compromising long-term cycling stability and safety. [27,28] These limitations highlight a fundamental trade-off: while physical crosslinking enables biocompatibility and dynamic properties, it fails to provide the environmental stability required for real-world

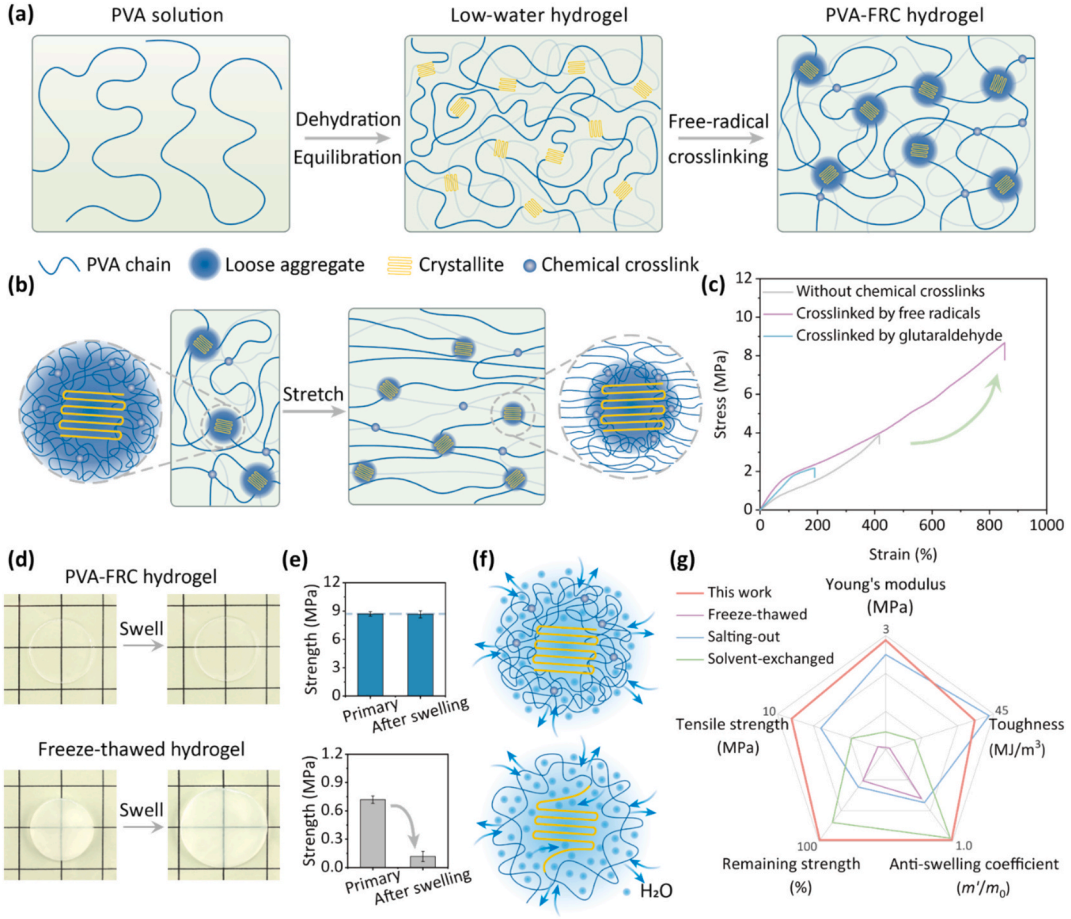

Fig. 1. Tough and anti-swelling PVA hydrogels via protective domains. a) Schematic of PVA-FRC fabrication: dehydration by air drying induces crystallization, followed by free radical crosslinking to form protective loose aggregates around crystallites. b) Deformation mechanism under tension: release of hidden chains enhances stretchability and energy dissipation. c) Tensile stress–strain curves of PVA hydrogels with different preparation. All three hydrogels are first dehydrated to form physical crosslinking. The "Without chemical crosslinks" sample is directly immersed in water, the "Crosslinked by free radicals" sample undergoes free radical crosslinking, and the "Crosslinked by glutaraldehyde" sample is chemically crosslinked with glutaraldehyde. d-f) Compared with freeze-thawed hydrogel, PVA-FRC hydrogel exhibits negligible variation in volume (d) and maintains its mechanical strength (e) after immersing in water, owing to the loose aggregates that effectively shield crystallites from water-induced dissociation (f). g) Radar plots showing superior overall performance of PVA-FRC hydrogels compared with other hydrogels prepared via freeze–thaw cycles, salting out,[19] and solvent exchange[37].

applications. In response, several design strategies have been proposed to suppress swelling, [29] such as incorporating hydrophobic crosslinkers [30] and constructing a denser network [31]. While these approaches help limit water absorption and enhance environmental stability, they often require complex synthetic processes or sacrifice other properties, including stretchability and water content.

To address these challenges, we propose a novel design strategy that constructs protective domains around processing-induced physical crosslinks to locally restrict network disruption. These protective domains, characterized by high chain density and chemical crosslinking, act as physical barriers that shield the noncovalent regions from solvent-induced destruction. Furthermore, the dense network chains within the protective domains can be gradually stretched during deformation, enabling the release of hidden molecular chains and providing additional extensibility and energy dissipation. [32] Herein, we demonstrate this concept using PVA as a model system due to its well-characterized ability to form both physical and chemical crosslinks. Our approach involves a two-step process (Fig. 1a): first, we induce controlled crystallization and chain aggregation through dehydration, creating a physically crosslinked network with high mechanical performance. Second, we perform homogeneous free-radical crosslinking (FRC) using potassium persulfate (KPS) and *N,N,N′,N′*-tetramethylethylenediamine (TMEDA), which penetrate the swollen network and introduce moderate chemical crosslinks. This process transforms loose polymer aggregates into protective domains that shield the crystallites from water-induced disruption while maintaining hidden chain length for energy dissipation. The resulting PVA-FRC (free radical crosslinking) hydrogels exhibit exceptional mechanical properties, including high modulus (~3 MPa), large stretchability (>850 %), and outstanding toughness (37 MJ/m^3), while demonstrating remarkable environmental stability with over 80 % strength retention and less than 5 % volume change after immersion in various challenging conditions including pure water, salt solutions, and extreme pH environments. This strategy is also generalizable to physical-crosslinked PVA hydrogels prepared by other common methods such as freeze-thawing, salting-out, and cononsolvency, providing an effective way to stabilize their microstructures. Leveraging these advantages, we further demonstrate the application as robust electrolytes in zinc-ion batteries, where the cell with PVA–FRC electrolyte enables stable cycling for over 2343 h without failure.

Results and discussion

Design and fabrication of protective domain-reinforced hydrogels

Conventional physically crosslinked hydrogels face a fundamental dilemma: the hydrogen bonds that provide mechanical strength are inherently vulnerable to water disruption. Rather than abandoning physical crosslinks, we developed a strategy to protect them by constructing chemically crosslinked domains around crystallites (**Fig. 1a**). Controlled dehydration drives PVA chains to form hydrogen-bonded crystallites through enhanced polymer–polymer interactions. During subsequent free-radical crosslinking, the dense network undergoes initial swelling that enables uniform penetration of initiators. The co-initiator TMEDA promotes KPS to generate free radicals at room temperature, which react with PVA chains to form carbon-center radicals that crosslink with neighboring chains. [33,34] Because the polymer chains surrounding crystallites remain highly concentrated and partially immobilized after dehydration, the local chain density and reduced mobility greatly increase the probability of radical chain collisions. Consequently, free radical crosslinking preferentially occurs in these chain-dense regions, generating a higher local crosslinking density around crystallites. This locally enhanced crosslinking naturally produces a microscopic gradient of crosslink density around crystallites, which is intrinsic to the formation of the protective-domain architecture. These chemically stabilized loose aggregates evolve into protective domains that prevent crystal dissociation and maintain the network framework. Unlike glutaraldehyde-based methods that often create inhomogeneous networks, [35,36] this free-radical approach produces macroscopically uniform crosslinking. As these crosslinks form, they capture polymer chains in their aggregated state around crystallites, creating protective domains that function as barriers preventing water molecules from accessing and disrupting the hydrogen bonds.

The protective domain architecture creates a hierarchical mechanical response (**Fig. 1b**). Crystallites serve as permanent crosslinks maintaining network integrity, while the surrounding loose aggregates store excess chain length. Under mechanical loading, these aggregates progressively unfold and release polymer chains, enabling large deformation without network failure. This mechanism produces hydrogels with high modulus (~3 MPa), large extensibility (>850 %), and exceptional toughness (37 MJ/m^3)—a combination rarely achieved in single-network systems (**Fig. 1c**). Notably, conventional glutaraldehyde crosslinking often leads to over-crosslinking and constrained chain motion, resulting in reduced elongation at break. In contrast, the free radical crosslinking adopted here establishes moderate and uniformly distributed chemical crosslinks that preserve chain mobility and even enhance extensibility through the release of hidden polymer chains. Environmental testing validates the protective domain concept. After prolonged immersion in water, salt solutions, or extreme pH conditions, the hydrogels retain > 80 % of their mechanical strength with < 5 % volume change (**Fig. 1d-g**). For comparison, we chose freeze-thawed PVA hydrogels as the control, since this method shares the same physical basis with dehydration by reducing available water, increasing polymer fraction, and inducing crystallite crosslinks. With this mechanistic similarity, freeze-thawed hydrogels provide the most appropriate reference, although they lose most strength under identical conditions (Fig. S1, Supporting Information). The protective domains successfully prevent competitive water molecules and ions from disrupting the crystallites, maintaining both network structure and mechanical performance. This approach demonstrates that preserving and protecting aggregation states offers a more effective route to environmental stability than attempting to eliminate them entirely.

Microstructural evidence for protective domain formation

Understanding how protective domains stabilize crystallites requires tracking the structural evolution from dehydrated to swollen states. We prepared three hydrogel states for comparison: the densely packed low-water PVA hydrogel (10 wt% water), the unprotected PVA-water hydrogel obtained by direct swelling, and the protected PVA-FRC hydrogel formed through free-radical crosslinking (**Fig. 2a**). All three maintain optical transparency, indicating nanoscale rather than macroscopic phase separation. However, their internal architectures differ dramatically. SEM reveals that while PVA-water exhibits large, vulnerable pores after swelling, PVA-FRC develops a closed-cell structure with reinforced walls—a direct consequence of protective domain formation that prevents excessive swelling and structural collapse. Notably, even after swelling, the water content in PVA-water hydrogel remains below the original solution concentration, demonstrating that dehydration creates irreversible chain aggregation (Fig. S2, Supporting Information).

Molecular and thermal analyses confirm that protective domains preserve the beneficial aggregation structures. FTIR spectroscopy reveals characteristic bands at 1141 and 1095 cm^{-1}, corresponding to crystalline and amorphous C–C stretching modes, respectively (**Fig. 2b**). [38] Upon swelling from low-water PVA to the PVA-water hydrogel, the 1141 cm^{-1} peak becomes essentially absent, indicating massive crystallite dissolution. In contrast, PVA-FRC preserves a discernible 1141 cm^{-1} feature, suggesting that chemical crosslinking effectively protects the crystalline structures from disruption. To compare the relative fractions of crystallites and loose aggregates while minimizing structural reorganization during drying, all hydrogels were first chemically locked by excess glutaraldehyde crosslinking before DSC analysis (see

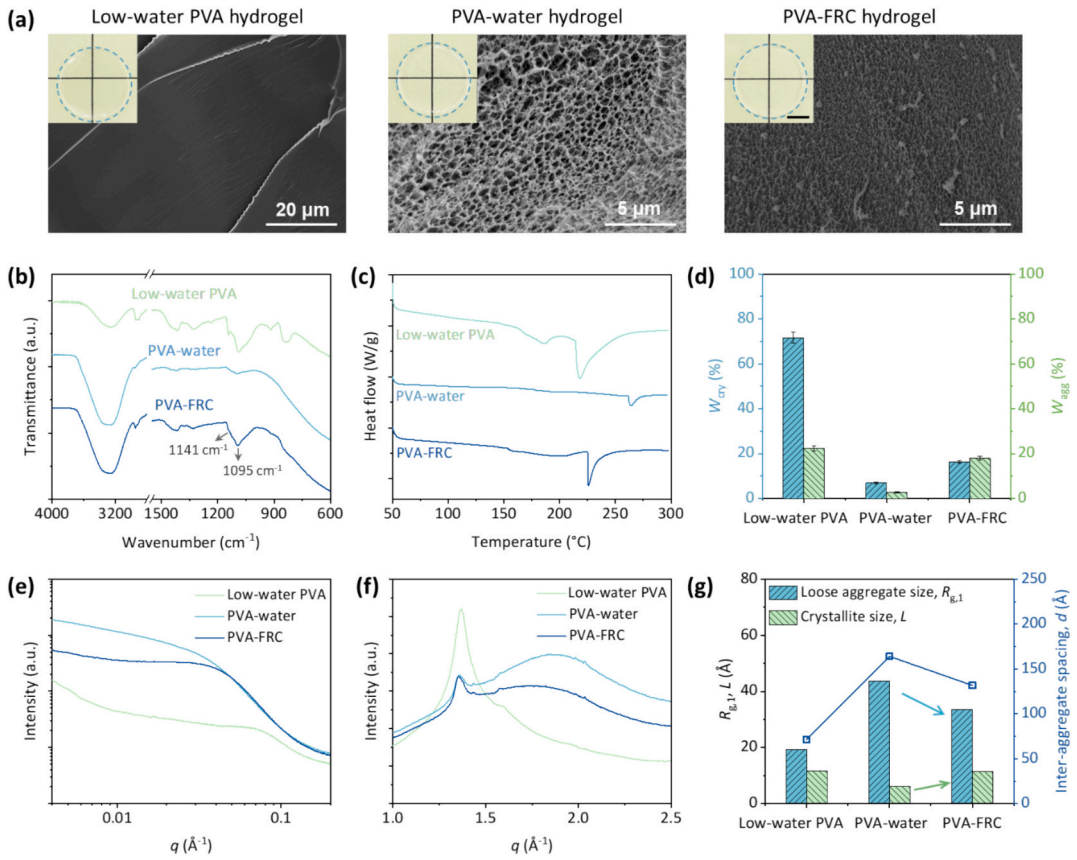

Fig. 2. Characterization of the microstructure and crystalline-associated domains of hydrogels. a) SEM images of all three hydrogels, showing the dense structure of low-water PVA hydrogel and closed-cell structure of PVA-water and PVA-FRC hydrogels. Insets are photos of the corresponding hydrogels. Scale bar: 5 mm. **b)** FI-TR spectra of low-water, PVA-water, and PVA-FRC hydrogels. **c)** DSC thermographs of all three hydrogels, showing sharp peak from the melting of crystalline domains and broad peak from the dissociation of loose aggregates. **d)** Mass fraction of crystallites, W_{cry}, and loose aggregates, W_{agg}, of all three hydrogels, calculated from the enthalpy values obtained in the DSC thermographs. **e-g)** SAXS profiles **(e)**, WAXS profiles **(f)** and corresponding average inter-aggregate spacing, d, loose aggregate size, $R_{g,1}$, and crystallite size, L, **(g)** of all three hydrogels.

Methods). This treatment preserves the aggregates and crystalline regions formed in the hydrated state. Therefore, the DSC results reflect the relative amounts and thermal stability of these pre-existing domains rather than drying-induced artifacts. The quantitative microstructural details in the native gel state were subsequently established through SAXS/WAXS measurements (Fig. 2e-g). DSC measurements are conducted to compare the thermal stability among different samples (Fig. 2c). Two distinct melting transitions appear: a broad peak at 200 °C from loose aggregates and a sharp peak at 225 °C from crystallites. The presence of both structures in PVA-FRC confirms our hypothesis—chemical crosslinks capture polymer chains in their aggregated state around crystallites. Interestingly, the unprotected PVA-water hydrogel shows a higher crystallite melting temperature (264 °C), indicating that surviving crystallites reorganize into more perfect structures during uncontrolled swelling. [39,40] In contrast, the presence of pre-formed aggregates and chemical crosslinks in PVA-FRC restricts chain diffusion and crystal perfection, leading to lower T_m values. Peak integration of the DSC traces enables a comparative estimation of the relative contents of crystalline and aggregated domains (Fig. 2d). The results indicate that while water infiltration destroys ~ 90 % of crystalline content in unprotected hydrogels (from 71.6 % to 6.9 %), chemical protection preserves substantial crystallites (16.3 %) and aggregation (18.0 %).

X-ray scattering provides nanoscale structural insights that validate the protective domain mechanism. [41] The SAXS profiles are fitted using the two-level Beaucage unified model over q = 0.004–0.20 Å^{-1} (Fig. 2e; Fig. S3, Table S1, Supporting Information). [42] The fractal dimension ($D \equiv P_1$) increases from 2.29 in low-water PVA to 3.99 in PVA-FRC, indicating that chemical crosslinking creates denser, more compact aggregates compared to the looser structures (D = 2.69) in PVA-water hydrogel. Despite similar water contents (~65 wt%), PVA-FRC shows significantly smaller inter-aggregate spacing (132 Å vs 164 Å), confirming a higher density of protective domains (Fig. 2g, Fig. S4, Supporting Information). The aggregate size ($R_{g,1}$) increases upon swelling due to chain uncoiling, but chemical crosslinking limits this expansion—PVA-FRC aggregates (33.5 Å) remain more compact than those in PVA-water (43.8 Å). [43] WAXS measurements show the opposite trend for crystallite size: PVA-FRC maintains larger crystallites (11.5 Å) compared to PVA-water (6.13 Å) (Fig. 2f). [44] This apparent contradiction—smaller aggregates but larger crystallites in PVA-FRC actually confirms the protective mechanism. Chemical crosslinks prevent aggregate loosening while preserving crystallite integrity, whereas unprotected systems experience partial crystallite dissolution and aggregate expansion (Fig. S5, Supporting Information). The discrepancy between SAXS (volume-based) and DSC (mass-based) measurements further confirms that PVA-FRC aggregates are indeed denser, providing effective protection for the embedded crystallites.

Mechanical performance and structural evolution during loading

Benefit from abundant crystallites serving as permanent crosslinks during deformation and loose aggregates dissipating energy through dissociation, the PVA-FRC hydrogel exhibits excellent toughness and stretchability simultaneously. Toughness, Γ, of PVA-FRC hydrogel

increases from 7.8 to 37.1 MJ/m^3, and the breaking strain, ε_b, increases from 404 % to 855 %, compared to the PVA-water hydrogel fabricated from the same low-water PVA hydrogel (Fig. 3a). The notable increase in stretchability is attributed to the stored length within loose aggregates which can be released during deformation. Besides, the appropriate and uniform chemical-crosslink density prevents the gel from premature network rupture caused by excessive crosslinking and stress concentration. Similarly, PVA-FRC hydrogel also shows remarkable Young's modulus (E = 2.88 MPa) and outstanding tensile strength (σ_b = 8.70 MPa), exceeding PVA-water hydrogel by 2.4 and 2.2 times, respectively. The dissociation of loose aggregates during stretching effectively dissipates energy through hydrogen-bond destruction and intermolecular friction.

The mechanical properties of both PVA-FRC and PVA-water hydrogels are highly dependent on the dehydration degree of low-water PVA hydrogels, which provides an effective way of regulation. As water content, q_0, increases from 10 to 30 wt%, E of low-water PVA hydrogels sharply decreases from 429 MPa to 120 MPa, and σ_b reduces from 304 to 125 MPa (Fig. S6, Supporting Information). Higher water content enhances polymer chain mobility, diminishing hydrogen-bond formation and reducing chain density, thus weakening the network. As a result, the mechanical properties decrease significantly, affecting the network formation of subsequent hydrogels. PVA-water hydrogel prepared from low-water PVA hydrogel with higher q_0 has lower crystallinity, resulting in the decreased mechanical properties with E dropping from 1.18 to 0.85 MPa and σ_b from 4.03 to 2.51 MPa when q_0 increases from 10 to 30 wt% (Fig. 3b; Fig. S7,S8, Supporting Information). Similarly, the mechanical properties of PVA-FRC hydrogels also decrease with increasing q_0 (E from 2.88 to 1.44 MPa and σ_b from 8.70 to 4.42 MPa, Fig. 3c). Even with higher q_0, substantial swelling allows for effective incorporation of free radical initiators, improving the stiffness and toughness relative to PVA-water hydrogels. In addition to regulating the dehydration degree, we also varied the concentrations of KPS and TMEDA to examine their influence on network formation (Fig. S9, Supporting Information). Increasing KPS leads to slightly higher modulus (E increases from 1.73 MPa at 1 wt% to 2.88 MPa at 4 wt%) and strength (σ_b increases from 7.5 MPa at 1 wt% to 8.7 MPa at 4 wt%) due to a modest rise in covalent crosslink density, whereas excessive TMEDA causes a slight reduction in extensibility (ε_b decreases from 855 % at 0.75 vol% to 570 % at 1.5 vol %) owing to over-crosslinking. However, the overall variation remains limited because the mechanical performance is primarily governed by the swelling-defined aggregation structure of the loose domains, and the free-radical crosslinking mainly serves to fix this pre-formed microstructure rather than fundamentally alter it.

To characterize the viscoelastic behavior of the hydrogel, the rheological properties of PVA-FRC hydrogel are investigated. The strain-sweep spectra of PVA-FRC hydrogel shows that the loss factor tan δ remains < 0.1 at the small strain and increases sharply to 0.4 when strain > 20 % (Fig. 3d). This indicates predominantly elastic behavior within the linear regime, and significant viscosity enhancement through loose aggregate dissociation at higher strains. Compared to PVA-water hydrogel (tan δ = 0.16), the higher tan δ of PVA-FRC implies more abundant and denser aggregates, which dissipate greater energy via hydrogen-bond destruction, chain sliding, and disentanglement (Fig. S10, Supporting Information). Additionally, PVA-FRC hydrogel exhibits delayed onset of nonlinear behavior (6.8 %) compared to PVA-water hydrogel (0.3 %), indicating that the chemical crosslinks in the PVA-FRC effectively prevent network from failure under loading and

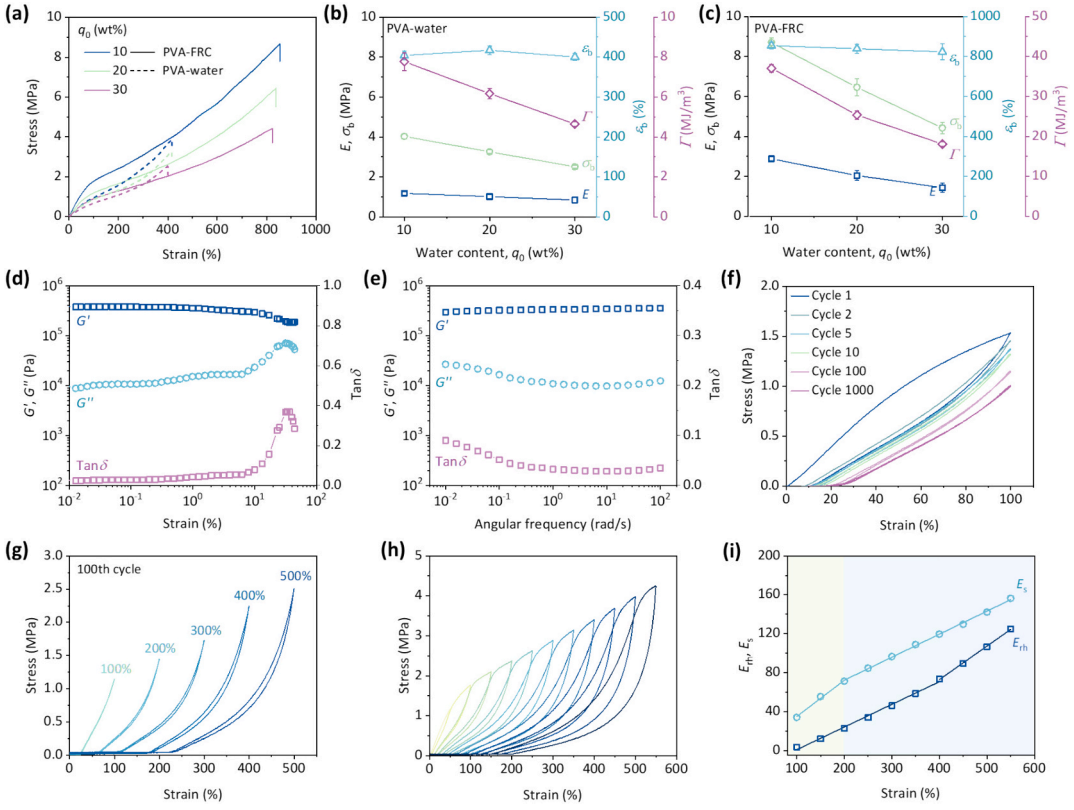

Fig. 3. Mechanical properties and energy dissipation behavior of PVA-FRC hydrogels. a-c) Tensile stress–strain curves **(a)** and corresponding Young's modulus, E, tensile strength, σ_b, breaking strain, ε_b, and toughness, Γ, of PVA-water **(b)** and PVA-FRC **(c)** hydrogels fabricated from low-water PVA hydrogel with different water content, q_0. **d,e)** Strain-sweep **(d)** and frequency-sweep **(e)** rheological spectra of storage modulus, G', loss modulus, G'', and loss factor, tan δ, for PVA-FRC hydrogels. **f)** Cyclic tensile stress–strain curves of PVA-FRC hydrogel under a fixed strain of 100%. **g)** Cyclic tensile stress–strain curves at various fixed strains after 100 successive loading–unloading cycles without internal. **h)** Sequential loading–unloading tensile curves with progressively increasing maximum strain. **i)** Energy losses of recovery hysteresis, E_{rh}, and Mullins softening, E_s, under different strains.

lead to superior mechanical resilience. The frequency-sweep spectra of PVA-FRC hydrogel shows that the storage modulus G' and loss modulus G'' remain almost constant, and the loss factor, tan δ, is small (< 0.1) in the observed frequency range ($10^{-2} < \omega < 10^{2}$ rad/s), indicating high elasticity and stability (Fig. 3e**)**. According to the formula: $G_e = NRT$, where G_e is the plateau modulus, R is gas content, T is the absolute temperature, the effective network density (N) can be calculated by the plateau storage modulus. [45,46] The results show that the N of PVA-FRC hydrogel (141 mol/m^3) is much higher than that of PVA-water hydrogel (17.7 mol/m^3), suggesting the former contains a high quantity of effective chains per unit volume of hydrogel. The synergistic effect of chemical crosslinks and crystalline-associated domains ensures most segments contribute to load-bearing capability, forming an integrated network with a high effective crosslinking density. In contrast, PVA-water hydrogel relies rarely on loose crystalline-associated domains, some of which undergo slippage and disintegration during loading and fail to function as stable crosslinking points, leading to a lower N than that of PVA-FRC hydrogel.

Cyclic tensile tests are performed under various fixed strains for 100 cycles to demonstrate the mechanical durability and structural evolution of the PVA-FRC hydrogels. Initially, significant hysteresis loops are observed during the first loading–unloading cycles at various fixed strains, indicating pronounced energy dissipation (Fig. 3f; Fig. S11, Supporting Information). From the second cycle onward, minimal hysteresis is observed, indicating that most structural damage occurs during the initial deformation. Subsequently, the hydrogel exhibited nearly pure elasticity with negligible hysteresis (Fig. 3g). Moreover, even after a 1200 s waiting time, the hysteresis loop remains negligible, confirming the irreversible nature of the initial damage (Fig. S12, Supporting Information). To quantify the energy dissipation and structural changes, the variations in hysteresis loop area and maximum stress during cyclic tests are analyzed at different strains (Fig. S13, Supporting Information). With increasing strain, the hysteresis loop after 100 cycles gradually increases, indicating enhanced energy dissipation during loading. Compared to load-unload cycles at strain of 100 %, the normalized stress after 100 cycles at 200 % showed a significant decrease, suggesting irreversible stress softening. In contrast, at strains above 200 %, the normalized stress remained relatively stable after 100 cycles, implying that major irreversible rearrangements (dissociation of loose aggregates) have already occurred and further deformation is predominantly accommodated by reversible structural adjustments (destruction of weak hydrogen bonds).

The observed phenomena in the cyclic tests are consistent with the typical Mullins effect, originally discovered in carbon black-filled natural rubber, characterized by irreversible structural damage leading to softening during initial cyclic loading while maintaining elasticity in subsequent cycles. [47,48] Typically reported in double-network or composite hydrogels, this effect is rarely seen in single-network systems. [49] To further investigate this strain-softening behavior, cyclic tensile tests under gradually increased maximum strains without internals are performed (Fig. 3h). These tests clearly display reduced stress at identical strains during subsequent loading cycles, while stresses recovered to levels consistent with monotonic tensile tests once the applied strain surpassed previous maximum extensions, indicating further structural damage occurring at strains larger than the previous maximum elongation. Energy losses of the recovery hysteresis (E_{rh}) and softening (E_s) are integrated from the cyclic tensile curves (Fig. 3i). E_{rh} is the area encircled by the preceding and subsequent loading curves, while E_s is the area encircled by the subsequent loading and the preceding unloading curves. E_s increases rapidly below 200 %, but slowly after reaching 200 %, corresponding to the before mentioned conclusion that irreversible structural damage due to aggregate dissociation primarily occurs below 200 %. Meanwhile, E_{rh} showed a continuous linear increase with strain, with a more pronounced acceleration observed above 400 %. This accelerated increase is attributed to strain hardening, which promotes reformation of hydrogen bonds, consistent with the strain hardening behavior identified by the Mooney-Rivlin equation (Fig. S14, Supporting Information). [50] Furthermore, the progressive unfolding mechanism inferred from the cyclic mechanical response is further validated through finite-element simulations (Fig. S15, Supporting Information). The simulated strain-field distribution reveals a clear hierarchical deformation sequence in which the amorphous matrix deforms first, followed by the progressive stretching and dissociation of the loose aggregates, while the crystallite domains remain minimally deformed throughout loading.

Protective domain mediated environmental stability

The PVA-FRC hydrogels exhibit remarkable environmental stability, attributable to a synergetic effect between loose aggregates and homogeneous chemical crosslinks that protect the crystallites. Even after immersion in pure water for an extended period, the hydrogel retains both macroscopic volume and mechanical properties, in contrast to the partial mechanical decrease often reported in PVA hydrogels fabricated from salting-out, freeze-thawed cycles, or cononsolvency methods (Fig. 1d-g, Fig. S16, Supporting Information). To evaluate the stability of PVA-FRC hydrogels in ionic environments, we further immerse the hydrogels in aqueous solutions containing various salting-in ions (e.g., NaCl, NaBr, $NaNO_3$, $MgCl_2$, and $CaCl_2$) for 5 days. Salting-in ions are known to preferentially interact with polymer chains, destroying the polymer–polymer hydrogen bonds via direct binding with hydroxyl groups and consequently enhancing polymer chain hydration and solubility (Fig. S17, Supporting Information). [19,51] As shown in Fig. 4a, the hydrogels retained their original size and transparency after 5 days of immersion in different salt solutions, with no visible morphological change. Interestingly, despite such disruptive potential, the modulus of the PVA-FRC hydrogels exhibited negligible variation, demonstrating the structurally protective effects from loose aggregates and chemical crosslinks, thus the robust crystallites effectively survive the destruction of salting-in ions (Fig. 4b). Nonetheless, a moderate decline in tensile strength is observed, particularly pronounced in solutions with stronger salting-in ions. For example, the tensile strength decreased from 8.5 MPa to approximately 7.0 MPa, 6.5 MPa, and 6.4 MPa after immersion in $NaNO_3$, $MgCl_2$, and $CaCl_2$ solutions, respectively (Fig. 4c). This weakening primarily manifests at a large strain, attributable to the partial dissociation of relatively weaker hydrogen bonds within loose aggregates, thus impairing the effectiveness of the aggregates to dissipate energy during substantial deformation.

Generally, in highly acidic or alkaline conditions, the crystallites within conventionally physical-crosslinking PVA hydrogels tend to degrade due to protonation or deprotonation of hydroxyl groups, thereby reducing the network integrity and weakening hydrogels. This leads to notable reductions in stiffness and toughness (Fig. S18, Supporting Information). However, PVA-FRC hydrogels display a remarkable resilience under these conditions, retaining their original size and transparency without visible morphological change (Figs. 4d,e). Although slight decreases in modulus and elongation are observed, these are significantly milder compared to traditional hydrogels (Fig. 4f). Together, these findings highlight the exceptional environmental stability of PVA-FRC hydrogels, making them particularly attractive for applications that demand sustained mechanical performance in aggressive chemical environments. Meanwhile, the hydrogel demonstrates reasonable thermal resistance because of the stable network. The temperature-sweep spectra show the storage modulus remains unchanged when the temperature increases from 10 to 50 °C (Fig. S19, Supporting Information). While a gradual increase in loss factor is observed above 60 °C due to the destruction of abundant hydrogen bonds, the overall network structure stays intact, indicating its suitability for applications under mildly elevated temperatures. The dehydration process facilitates robust hydrogen-bond interactions among the polymer chains by minimizing competitive interactions from water molecules. Besides, the following formation of chemical crosslinks

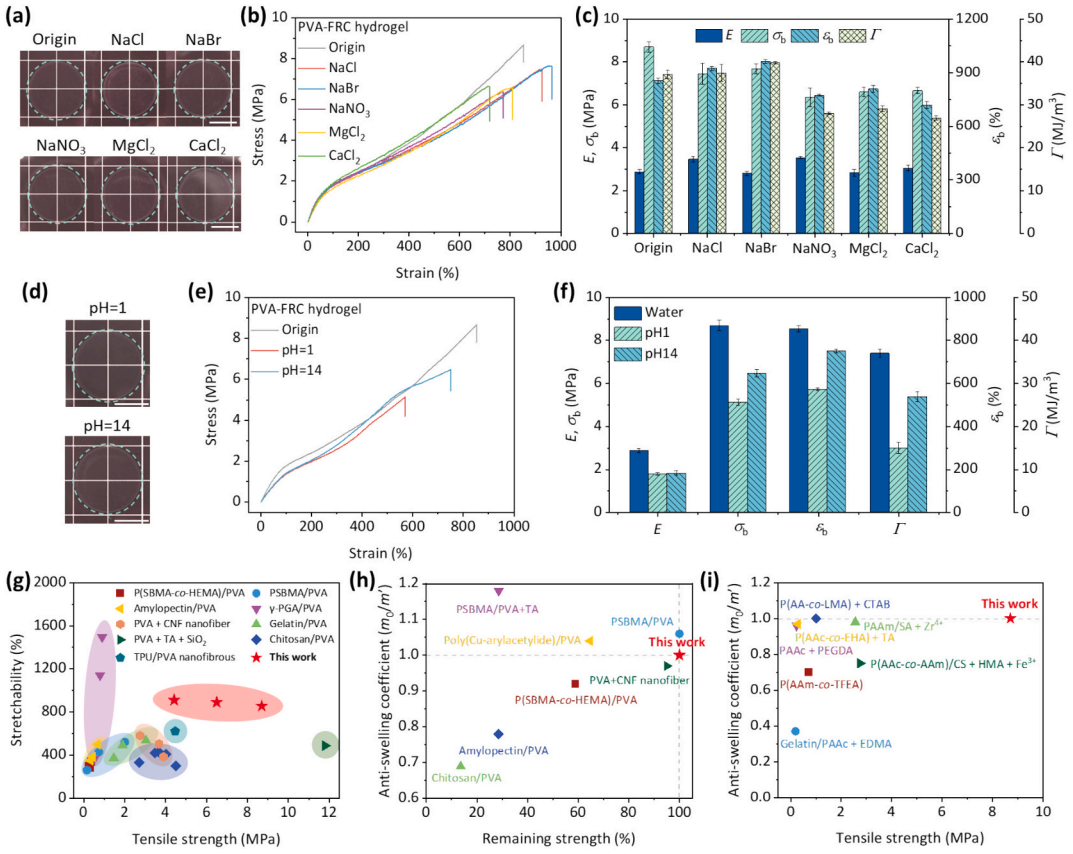

Fig. 4. Environmental stability and anti-swelling performance of PVA-FRC hydrogel. a-c) Photos **(a)**, tensile stress–strain curves **(b)** and corresponding Young's modulus, E, tensile strength, σ_b, breaking strain, ε_b, and toughness, Γ, **(c)** of PVA-FRC hydrogels after swelling in various salting-in solutions (NaCl, NaBr, $NaNO_3$, $MgCl_2$, $CaCl_2$) for 5 days. **d-f)** Photos **(d)**, tensile stress–strain curves **(e)** and corresponding parameters **(f)** of PVA-FRC hydrogels after swelling in different pH solutions (pH = 1, 14) for 5 days. **g,h)** Comparison of mechanical properties, stretchability versus tensile strength **(g)**, and anti-swelling properties, remaining strength versus anti-swelling coefficient (m_0/m') **(h)**, of PVA-FRC hydrogel in this work and other reported PVA-based anti-swelling hydrogels. **i)** Comparison of anti-swelling coefficient versus tensile strength of PVA-FRC hydrogel in this work and previously reported non-PVA anti-swelling hydrogels.

restricts chain mobility, making the resulting network less susceptible to thermal disruption. Consequently, the pre-established hydrogen bonds formed under dehydration persist and are effectively shielded by the chemical crosslinking. As shown in Figs. 4g,h, the PVA-FRC hydrogel developed in this work achieves a great balance between tensile strength and stretchability, and simultaneously maintains its volume and tensile strength after immersion compared to previously reported PVA-based anti-swelling hydrogels (Table S2, Supporting Information). Fig. 4i further extends this comparison to non-PVA anti-swelling hydrogels, showing that the PVA-FRC hydrogel also exhibits competitive performance in terms of both robustness and swelling resistance (Table S3, Supporting Information).

Generality of the stabilization strategy across various architectures

To demonstrate the broad applicability of this stabilization strategy, which relies on the formation of loose aggregates around crystallites, we systematically applied it to three representative PVA hydrogel systems: freeze-thawed (Fig. 5a-c), salting-out (Fig. 5d-f), and cononsolvency (Fig. 5g-i). Although these conventional methods can induce physical crosslinking through hydrogen bonds and crystallites, the crosslinking domains are directly exposed to the environment and thus highly susceptible to disruption by water molecules, ions, or pH variations. As a result, their microstructural stability and mechanical performance often deteriorate severely under environmental stimuli. Our approach addresses a critical limitation in conventional hydrogels, where microstructural stability is often compromised by environmental triggers. Freeze-thawed PVA hydrogel typically exhibit pore structures due to ice-templating, but its mechanical properties decrease significantly after swelling in water. After dehydration and free radical crosslinking (D-FRC), the treated hydrogel shows a much smaller swelling ratio (decreases from 1.29 to 1.03; Fig. 5a). The walls of pores become more dense and complete compared to that before treatment, leading to an increase in tensile strength (from 36 to 122 kPa) and stretchability (from 230 to 285 %) (Fig. 5c; Fig. S20,S21, Supporting information). Salting-out effect induces chain aggregation via ion-mediated dehydration in saline solution, but subsequent rehydration in water disrupts hydrogen bonds, causing volume expansion and mechanical decay. The swelling ratio of untreated salting-out hydrogel is 1.2 when it transfers from saturated Na_2SO_4 solution to water, accompanying strength reduction from 1.26 to 0.33 MPa. (Figs. 5d, f). The D-FRC treatment can effectively inhibit the dissociation of hydrogen-bond crystallites, leading to a smaller swelling ratio in water (1.01) and almost unchanged modulus (~0.45 MPa) without the expense of pore structure. Cononsolvency hydrogel which is formed by mixing PVA/H_2O and PVA/DMSO solution, is susceptible to collapse induced by solvent exchange. After D-FRC treatment, the swelling ratio decreased from 1.13 to 1.02 (Fig. 5g), and tensile strength retention improved dramatically (from 11 % to 74 % of its original strength; Fig. 5i). The treatment also preserves the original pore architecture without collapse, as confirmed by SEM image. In summary, this stabilization strategy containing dehydration and free radical crosslinking process improves the stability of hydrogels without compromising their intrinsic architectures. This versatility shows the potential of this strategy for designing hydrogels with application-tailored microstructures and environmental resilience.

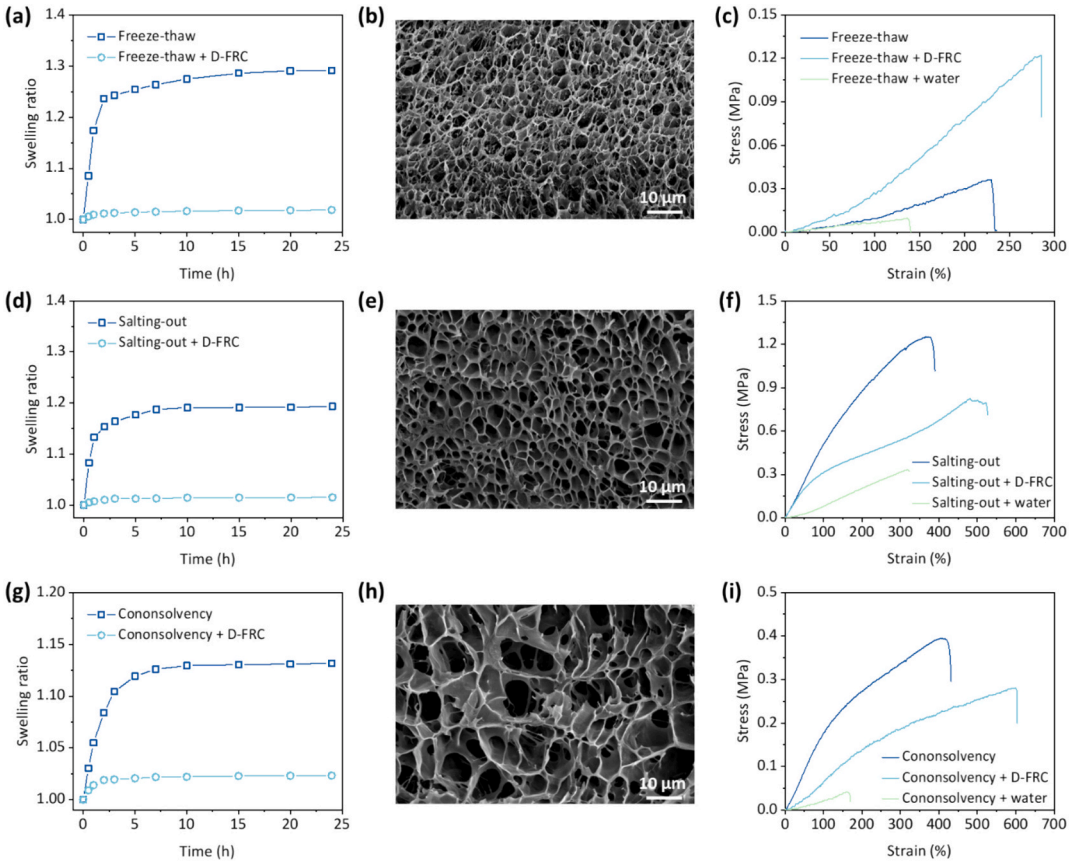

Fig. 5. Generality in stabilizing various architectures of PVA hydrogels. a-c) Swelling ratio **(a)**, SEM image **(b)**, and tensile stress–strain curves **(c)** of PVA hydrogel prepared by freeze-thawing 3 cycles, after dehydration-free radical crosslinking (D-FRC) treatment. **d-f)** Swelling ratio **(d)**, SEM image **(e)**, and tensile stress–strain curves **(f)** of PVA hydrogel prepared by salting-out in saturated Na_2SO_4 solution, followed by D-FRC treatment. **g-i)** Swelling ratio **(g)**, SEM image **(h)**, and tensile stress–strain curves **(i)** of cononsolvency-induced PVA hydrogel prepared by mixing PVA/H_2O and PVA/DMSO, followed by D-FRC treatment.

Protective domain engineered hydrogels for stable Zn cycling

Hydrogels are attractive electrolytes for zinc-ion batteries due to high ionic conductivity, flexibility, and good interfacial compatibility, but uncontrolled dendrite growth severely compromises their cycling stability and lifespan. [52–54] Zinc trifluoromethanesulfonate (Zn(OTF)$_2$) based electrolytes can mitigate dendrite formation because the bulky triflate anions regulate Zn^{2+} solvation and deposition kinetics, leading to more uniform ion flux and smoother Zn plating. [55,56] However, the OTF^- anion is known to impose a pronounced salting–in effect on PVA chains, causing conventional PVA hydrogels to severely swell and mechanically degrade after immersion, which undermines their ability to mitigate dendrite formation on Zn anodes. [57] In contrast, owing to its protective domains (chemically crosslinked loose aggregates surrounding crystallites), the PVA–FRC hydrogel preserves network integrity and mechanical performance after immersion in 1 M Zn(OTF)$_2$ (Fig. S22, Supporting Information), thereby providing a stable, uniform ionic–transport medium together with a mechanically resilient barrier that regulates Zn deposition and supports reversible plating/stripping.

In Zn//Zn symmetric cells, conventional freeze–thawed (F–T) PVA hydrogels fail within ~ 260 h due to uncontrolled dendritic growth, whereas cells using the PVA–FRC electrolyte sustain cycling for at least 2343h, indicating that the mechanically resilient network effectively regulates Zn deposition (Fig. 6a; Fig. S23, Supporting Information). The stabilized transport environment yields the strong rate performance: as current density increases stepwise from 1 to 10 mA/cm^2, the overpotential rises only slightly from 0.10 to 0.20 V (Fig. 6b). Long–term operation at 5 mA/cm^2 with a 17.3 % depth of discharge maintains a stable voltage profile (Fig. S24, Supporting Information). Zn//Cu cells with PVA–FRC deliver a high average Coulombic efficiency of 99.8 %, evidencing highly reversible Zn plating/stripping. (Fig. 6c). The slightly higher values observed in the initial cycles likely originate from electrode surface activation, before stabilizing near 100 %. To rationalize this reversibility, we quantified ion transport after immersion: the ionic conductivity of PVA–FRC is 19.6 mS/cm, markedly higher than that of F–T PVA (4.2 mS/cm; Fig. 6d), and the Zn^{2+} transference number reaches 0.54 (Fig. S25, Supporting Information), indicating fast transport with a preferential Zn^{2+} contribution that mitigates concentration polarization and promotes uniform deposition. Finally, Zn//PANI full cells using PVA–FRC exhibit superior cycling, retaining ~ 100 % Coulombic efficiency for > 1007 cycles at 0.038 mA/cm^2 (Fig. 6e). The initially lower efficiencies observed in the first 10 cycles can be ascribed to electrode activation and the gradual formation of an interfacial layer, after which the Coulombic efficiency stabilizes near 100 %.

Conclusion

In conclusion, we have developed a simple and generalizable strategy to construct tough and environmentally stable PVA hydrogels by forming protective domains around crystallites via sequential dehydration and free-radical crosslinking. The protective domains, realized as loose aggregates surrounding crystallites, are formed through polymer chain aggregation and chemical crosslinking. These structures effectively shield the crystallites and stabilize the network under swelling conditions. As a result, the resulting PVA-FRC hydrogels exhibit remarkable mechanical performance and outstanding resistance to salting-in ions, extreme pH, and elevated temperatures, while

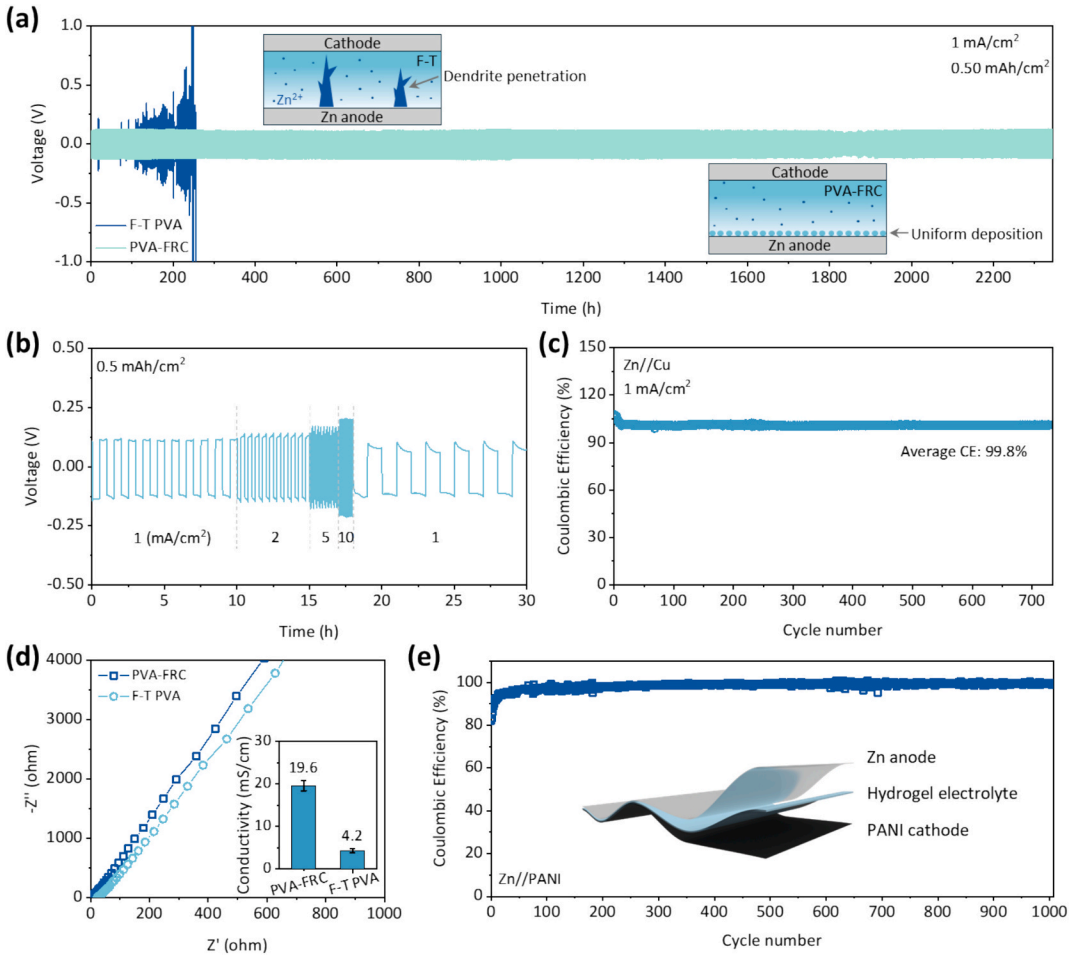

Fig. 6. Electrochemical performance of zinc-ion batteries with PVA-FRC electrolyte. a) Cycling performance of the Zn//Zn cells with PVA-FRC and Freeze-thawed PVA (F-T PVA) electrolytes at a current density of 1 mA/cm^2. **b)** Rate performance of the Zn//Zn cells with PVA-FRC electrolyte. **c)** Coulombic efficiency of Zn//Cu cells with PVA-FRC hydrogel at a current density of 1 mA/cm^2. **d)** Electrochemical impedance spectroscopy (EIS) curves and corresponding ionic conductivity (inset) of different electrolytes. **e)** Coulombic efficiency of Zn//PANI cells. Inset is the scheme of a pouch cell.

maintaining minimal volume swelling. Under loading, the hydrogel undergoes a two-stage structural evolution. In the first stage, the loose aggregates irreversibly dissociate, dissipating abundant energy and inducing Mullins softening, while simultaneously releasing hidden chain length to enable large stretchability. In the second stage, internal hydrogen bonds within loose aggregates dynamically break and reform, sustaining further deformation without failure. This sequential mechanism, irreversible aggregate dissociation followed by reversible bond rearrangement, endows the hydrogel with both toughness and resilience. This stabilization strategy proves applicable to diverse physically crosslinked PVA architectures (e.g., freeze-thawed, salting-out, cononsolvency), highlighting its universality and potential for constructing high-performance hydrogels in demanding environments. The zinc-ion batteries fabricated with the PVA–FRC hydrogel successfully cycled for more than 2343 h, demonstrating its promise as a robust electrolyte for practical energy storage applications.

Materials and methods

Materials

Poly(vinyl alcohol) (PVA) (weight-average molecular weight of 89–98 kDa; degree of hydrolysis of 99 %), potassium persulfate (KPS, ACS reagent), *N,N,N′,N′*-tetramethylethylenediamine (TMEDA, 99 %), glutaraldehyde (GA, 25 %), hydrochloric acid (HCl, 36.5–38 %), sodium sulfate (ACS reagent) were purchased from Sigma-Aldrich. Dimethyl sulfoxide (DMSO, Certified ACS) was purchased from Fisher chemical. Millipore deionized water was used for all solution preparations and sample treatments.

Fabrication of hydrogels

PVA-FRC hydrogels were fabricated via a two-step process. First, 20 wt% PVA aqueous solution was prepared by dissolving PVA in deionized water under vigorous stirring at 95 °C for 1 h. After removal of bubbles by centrifugation (2000 rpm, 120 s), 15 mL of solution was poured into a 5 cm-diameter Petri dish and exposed to air at room temperature for several days to allow gradual dehydration, reaching desired water contents (10, 20, or 30 wt%) as determined by gravimetric analysis. The resulting low-water PVA gels (~0.5 mm thickness) were sealed in vacuum bags for 3 days to homogenize water distribution. PVA-FRC hydrogel was prepared by incubating the low-water PVA hydrogel into 50 mL aqueous solution containing 4 wt% KPS and 0.75 vol% TMEDA for 4 h to initiate free radical crosslinking. PVA-water hydrogel was prepared by simply immersing low-water PVA hydrogel into water for 3 days.

The traditional chemical crosslinking PVA-GA hydrogel as shown in Fig. 1c was prepared by incubating low-water PVA hydrogel (10 wt% water content) into 50 mL aqueous solution containing 10 mL GA and 0.1 mL HCl for 4 h to trigger acetal-bond formation as chemical crosslinking. The reacted hydrogel was transferred to a large amount of water to remove residuals for 3 days.

Freeze-thawed PVA hydrogel was prepared by pouring 10 wt% PVA solution into a Petri dish and freeze-thawed for 3 cycles. The freeze-thawed PVA hydrogel was air-dried to reach 80 wt% water content and then subjected to KPS/TMEDA solution as described above. Cononsolvency PVA hydrogel was fabricated by mixing 40 mL PVA DMSO solution (10 wt%) and 60 mL PVA H_2O solution (10 wt%), followed by centrifugation at 2,000 rpm for 120 s to remove the bubbles. The mixture was poured into a Petri dish and frozen at −20 °C for 12 h to form the hydrogel. The cononsolvency hydrogel was air-dried to reduce the water content to 20 wt%, then soaked in the KPS/TMEDA solution for 4 h for free radical crosslinking. Salting-out PVA hydrogel was prepared by freezing 10 wt% PVA aqueous solution at −20 °C for 12 h, followed by soaking in saturated sodium sulfate solution for 24 h. Without further drying, the shrunken hydrogel was directly crosslinked in KPS/TMEDA solution for 4 h. Unless otherwise specified, all FRC-treated hydrogels were immersed in deionized water for 3 days before characterization to remove residual chemicals.

Mechanical tests

Uniaxial and cyclic tensile tests were performed on dog-bone shaped specimens with a gauge length of 5 mm and a width of 2 mm using a Cellscale Univert mechanical tester. A minimum of three parallel tests were performed for each test to ensure reproducibility. All uniaxial and cyclic tensile tests, except for the low-water PVA sample, were conducted with the specimens fully immersed in deionized water to prevent dehydration. All samples exhibited negligible mass change after testing. The engineering stress–strain curves were calculated based on the initial gauge cross-section area and gauge length. All tests were performed at a constant loading rate of 0.5 mm/s.

Rheological characterizations

The rheological behaviors of hydrogels were measured using a TA Instrument Discovery HR-30 rheometer. Disk-like hydrogel samples with a diameter of 15 mm were placed between the parallel plate and the rheometer, with the edges sealed using water to prevent solvent evaporation from the gel. Strain sweeps were performed with a frequency of 1 rad/s at 25 °C. Temperature sweeps were conducted at a constant strain of 0.1 % and frequency of 1 rad/s, with a heating rate of 15 °C/min. Frequency sweeps were performed with a strain amplitude of 0.1 % at 25 °C.

Scanning electron microscopy (SEM)

The microstructures of hydrogels were observed with a FEI Teneo scanning electron microscope at 10 kV. The samples were prepared by freeze-drying and then cryogenically fractured in liquid nitrogen prior to imaging.

Fourier transform infrared spectroscopy (FTIR)

FTIR spectra were recorded at room temperature using an attenuated total reflectance mode (ATR-FTIR, Nicolet Summit X , Thermo Scientific). Each spectrum was averaged from 10 scans over the range of 4000–400 cm^{-1}.

Differential scanning calorimetry (DSC)

The hydrogels were treated with a 50 mL aqueous solution containing 30 mL glutaraldehyde (10 wt%) and 0.5 mL of hydrochloric acid for 3 h, followed by immersing in plenty of water to remove residuals. The samples were subsequently dried before DSC analysis. Measurements were performed using a TA Instruments Q2000 calorimeter with a heating rate of 15 °C/min from 50 °C to 300 °C after 2 min of equilibration.

Small- and wide-angle X-ray scattering characterization (SAXS/WAXS)

SAXS and WAXS measurements were carried out at the 12-ID-B beamline of Advanced Photon Source (Argonne National Laboratory) equipped with an Eiger2 9 M detector for SAXS and a Pilatus 300 K detector for WAXS. The wavelength of the X-rays was 0.932 Å. Sample-to-detector distances were 1995 mm for SAXS and 421 mm for WAXS. 2D scattering SAXS/WAXS patterns were azimuthally averaged to 1D curves and followed by background-subtraction using the beamline developed Matlab program. SAXS profiles were fitting using SasView with two-level Beaucage unified model over $q = 0.004 \sim 0.20$ Å^{-1}. [42] The function is:

$$I(q) = background + \sum_{i=1}^{2}\left[G_i exp\left(-\frac{q^2R_{g,i}^2}{3}\right) + B_i exp\left(-\frac{q^2R_{g,i+1}^2}{3}\right)\left(\frac{1}{q_i^*}\right)^{P_i}\right]$$

with

$$q_i^* = q\left[erf\left(\frac{qR_{g,i}}{\sqrt{6}}\right)\right]^{-3}$$

where $R_{g,i}$ is radius of gyration, G_i is Guinier prefactor, B_i is Porod prefactor, and P_i is Porod exponent. In this work, we interpret $R_{g,1}$ as the characteristic size of the loose aggregates. $R_{g,2}$ is fixed at 5000 Å, serving as a power-law background that extends into the higher-q region. From WAXS data curves, the crystallite size, L, is estimated by Scherrer equation:

$$L = \frac{K\lambda}{\beta cos\theta}$$

where K is shape factor (0.9), λ is X-ray wavelength (0.932 Å), β is the full width at half maximum, and θ is the Bragg angle calculated from $\theta = arcsin\frac{q\lambda}{4\pi}$ (q corresponds to the peak position in WAXS curves).

Electrochemical analysis

The basic electrochemical analyses were performed using a coin-cell system. Electrochemical impedance spectroscopy (EIS) was performed at 25°C using CHI660e electrochemical workstation (CH Instruments) using electrochemical impedance spectroscopy mode. The resistance was the interception on the real axis in the Nyquist plot at high frequencies, and the ionic conductivity (σ) was calculated as $\sigma = \frac{t}{R} \times A$, where t is the membrane thickness and A is the electrode area (1.77 cm^2). The coin cells were assembled with a TMAXCN hydraulic crimping machine with 1000 psi pressure and were tested with a LANDT CT3002AU battery tester.

CRediT authorship contribution statement

Hao Nan Qiu: Writing – review & editing, Writing – original draft, Visualization, Validation, Investigation, Formal analysis, Data curation, Conceptualization. **Chuan Wei Zhang:** Writing – review & editing, Formal analysis, Data curation, Conceptualization. **Lixin Dai:** Writing – review & editing, Resources, Formal analysis, Data curation. **Yichen Yan:** Writing – review & editing, Data curation. **Ping He:** Writing – review & editing, Data curation. **Ruoyi Ke:** Writing – review & editing, Data curation. **Xiaobing Zuo:** Writing – review & editing, Resources, Funding acquisition, Formal analysis. **Hua Zhou:** Writing – review & editing, Resources, Funding acquisition, Formal analysis. **Ximin He:** Writing – review & editing, Writing – original draft, Supervision, Resources, Project administration, Funding acquisition, Conceptualization.

Declaration of competing interest

The authors declare that they have no known competing financial interests or personal relationships that could have appeared to influence the work reported in this paper.

Acknowledgements

This research was supported by the American Chemical Society for award 66747-ND7, Johnson & Johnson for award 20231448, Inventor Fellow award 12072, NIH for award R01DK132319, the Moore Foundation Award 12072, Semiconductor Research Corporation for award 2023-JU3136, and the Office of Naval Research (ONR) for awards N000142412187 and N000142212595. This research was performed on APS beam time award (DOI: DOI: 10.46936/APS-189597/60013778) from the Advanced Photon Source, a U.S. Department of Energy (DOE) Office of Science user facility operated for the DOE Office of Science by Argonne National Laboratory under Contract No. DE-AC02-06CH11357.

Appendix A. Supplementary data

Supplementary data to this article can be found online at https://doi.org/10.1016/j.mattod.2025.12.005.

Data availability

All data are available within the article or Supplementary data.

References

[1] X. Zhao, Multi-scale multi-mechanism design of tough hydrogels: building dissipation into stretchy networks, Soft Matter 10 (2014) 672–687, https://doi.org/10.1039/C3SM52272E.
[2] X. Kong, et al., Tissue-compatible and lubricated hydrogel catheter with promising activity against polymicrobial infections for ventilator-associated pneumonia prevention, Adv. Healthc. Mater. 13 (2024) 2401750, https://doi.org/10.1002/adhm.202401750.
[3] H. Yuk, J. Wu, X. Zhao, Hydrogel interfaces for merging humans and machines, Nat. Rev. Mater. 7 (2022) 935–952, https://doi.org/10.1038/s41578-022-00483-4.
[4] Q.L. Zhu, et al., Closed twisted hydrogel ribbons with self-sustained motions under static light irradiation, Adv. Mater. 36 (2024) 2314152, https://doi.org/10.1002/adma.202314152.
[5] C.W. Zhang, et al., Supramolecular hydrogel actuators with reprogrammable magnetic orientation by locally mediated viscoelasticity and pinning force, Sci. Adv. 11 (2025) eadw0500. https://www.science.org/doi/full/10.1126/sciadv.adw0500.
[6] P. Li, et al., N-type semiconducting hydrogel, Science 384 (2024) 557–563, https://doi.org/10.1126/science.adj4397.
[7] Z. Wu, et al., A humidity-resistant, sensitive, and stretchable hydrogel-based oxygen sensor for wireless health and environmental monitoring, Adv. Funct. Mater. 34 (2024) 2308280, https://doi.org/10.1002/adfm.202308280.
[8] M. Wang, et al., Glassy gels toughened by solvent, Nature 631 (2024) 313–318, https://doi.org/10.1038/s41586-024-07564-0.
[9] S. Wang, et al., Strong, tough, ionic conductive, and freezing-tolerant all-natural hydrogel enabled by cellulose-bentonite coordination interactions, Nat. Commun. 13 (2022) 3408, https://doi.org/10.1038/s41467-022-31109-8.
[10] J.P. Gong, et al., Double-network hydrogels with extremely high mechanical strength, Adv. Mater. 15 (2003) 1155–1158, https://doi.org/10.1002/adma.200304907.
[11] Z.J. Wang, et al., Rapid self-strengthening in double-network hydrogels triggered by bond scission, Nat. Mater. 24 (2025) 607–614, https://doi.org/10.1038/s41563-025-02137-6.
[12] S.Y. Zheng, et al., Molecularly engineered zwitterionic hydrogels with high toughness and self-healing capacity for soft electronics applications, Chem. Mater. 33 (2021) 8418–8429, https://doi.org/10.1021/acs.chemmater.1c02781.
[13] J. Hao, R.A. Weiss, Viscoelastic and mechanical behavior of hydrophobically modified hydrogels, Macromolecules 44 (2011) 9390–9398, https://doi.org/10.1021/ma202130u.
[14] X. Guo, et al., Strong and tough fibrous hydrogels reinforced by multiscale hierarchical structures with multimechanisms, Sci. Adv. 9 (2023) eadf7075. https://www.science.org/doi/10.1126/sciadv.adf7075.
[15] J.-Y. Sun, et al., Highly stretchable and tough hydrogels, Nature 489 (2012) 133–136, https://doi.org/10.1038/nature11409.
[16] X. Li, J.P. Gong, Design principles for strong and tough hydrogels, Nat. Rev. Mater. 9 (2024) 380–398, https://doi.org/10.1038/s41578-024-00672-3.
[17] S. Lin, et al., Anti-fatigue-fracture hydrogels, Sci. Adv. 5 (2019) eaau8528. https://www.science.org/doi/full/10.1126/sciadv.aau8528.
[18] X. Bao, et al., Unusually long polymers crosslinked by domains of physical bonds, Nat. Commun. 16 (2025) 4749, https://doi.org/10.1038/s41467-025-59875-z.
[19] S. Wu, et al., Poly(vinyl alcohol) hydrogels with broad-range tunable mechanical properties via the Hofmeister effect, Adv. Mater. 33 (2021) 2007829, https://doi.org/10.1002/adma.202007829.
[20] M. Hua, et al., Strong tough hydrogels via the synergy of freeze-casting and salting out, Nature 590 (2021) 594–599, https://doi.org/10.1038/s41586-021-03212-z.
[21] H.N. Qiu, et al., Formation and destruction of polyelectrolyte/surfactant complexes for the toughening of hydrogels, Macromolecules 56 (2023) 8887–8898, https://doi.org/10.1021/acs.macromol.3c01742.
[22] J.Y. Hu, et al., Solvent exchange-induced microphase separation and structural arrest to form glassy hydrogels, Macromolecules 57 (2024) 11007–11019, https://doi.org/10.1021/acs.macromol.4c01758.
[23] Y. Alsaid, et al., Tunable sponge-like hierarchically porous hydrogels with simultaneously enhanced diffusivity and mechanical properties, Adv. Mater. 33 (2021) 2008235, https://doi.org/10.1002/adma.202008235.
[24] J. Wu, et al., Entropy-mediated polymer-cluster interactions enable dramatic thermal stiffening hydrogels for mechanoadaptive smart fabrics, Angew. Chem. Int. Ed. 61 (2022) e202204960, https://doi.org/10.1002/anie.202204960.
[25] H.M. El-Husseiny, et al., Smart/stimuli-responsive hydrogels: Cutting-edge platforms for tissue engineering and other biomedical applications, Mater. Today Bio 13 (2022) 100186, https://doi.org/10.1016/j.mtbio.2021.100186.
[26] C.W. Zhang, et al., Hierarchical engineering for biopolymer-based hydrogels with tailored property and functionality, Adv. Mater. 37 (2025) 2414897, https://doi.org/10.1002/adma.202414897.
[27] V. Vandeginste, J. Wang, A review of the synthesis of biopolymer hydrogel electrolytes for improved electrode-electrolyte interfaces in zinc-ion batteries, Energies 17 (2024) 310, https://doi.org/10.3390/en17020310.
[28] Y. Guo, et al., Molecular engineering of hydrogels for rapid water disinfection and sustainable solar vapor generation, Adv. Mater. 33 (2021) 2102994, https://doi.org/10.1002/adma.202102994.
[29] M. Li, et al., Water-induced phase separation for anti-swelling hydrogel adhesives in underwater soft electronics, Adv. Sci. 10 (2023) 2304780, https://doi.org/10.1002/advs.202304780.
[30] H. An, et al., Hydrophobic cross-linked chains regulate high wet tissue adhesion hydrogel with toughness, anti-hydration for dynamic tissue repair, Adv. Mater. 36 (2024) 2310164, https://doi.org/10.1002/adma.202310164.
[31] L. Xu, et al., A transparent, highly stretchable, solvent-resistant, recyclable multifunctional ionogel with underwater self-healing and adhesion for reliable strain sensors, Adv. Mater. 33 (2021) 2105306, https://doi.org/10.1002/adma.202105306.
[32] B. Huang, S. Nian, L.-H. Cai, A universal strategy for decoupling stiffness and extensibility of polymer networks, Sci. Adv. 10 (2024) eadq3080. https://www.science.org/doi/10.1126/sciadv.adq3080.
[33] F. Li, et al., From the accelerated production of •OH radicals to the crosslinking of polyvinyl alcohol: the role of free radicals initiated by persulfates, Appl. Catal. B Environ. 285 (2021) 119763, https://doi.org/10.1016/j.apcatb.2020.119763.
[34] A. Gupta, et al., Synthesis, characterization and efficacy of chemically crosslinked PVA hydrogels for dermal wound healing in experimental animals, J. Appl. Polym. Sci. 111 (2009) 1400–1408, https://doi.org/10.1002/app.28990.
[35] K.C.S. Figueiredo, T.L.M. Alves, C.P. Borges, Poly(vinyl alcohol) films crosslinked by glutaraldehyde under mild conditions, J. Appl. Polym. Sci. 111 (2009) 3074–3080, https://doi.org/10.1002/app.29263.
[36] C.-K. Yeom, K.-H. Lee, Pervaporation separation of water-acetic acid mixtures through poly(vinyl alcohol) membranes crosslinked with glutaraldehyde, J. Membr. Sci. 109 (1996) 257–265, https://doi.org/10.1016/0376-7388(95)00196-4.
[37] L. Xu, et al., A solvent-exchange strategy to regulate noncovalent interactions for strong and antiswelling hydrogels, Adv. Mater. 32 (2020) 2004579, https://doi.org/10.1002/adma.202004579.
[38] E. Fathi, et al., Physically crosslinked polyvinyl alcohol-dextran blend xerogels: Morphology and thermal behavior, Carbohyd. Polym. 84 (2011) 145–152, https://doi.org/10.1016/j.carbpol.2010.11.018.
[39] Y. Wu, et al., Solvent-exchange-assisted wet annealing: a new strategy for superstrong, tough, stretchable, and anti-fatigue hydrogels, Adv. Mater. 35 (2023) 2210624, https://doi.org/10.1002/adma.202210624.
[40] J.S. Gonzalez, V.A. Alvarez, The effect of the annealing on the poly(vinyl alcohol) obtained by freezing-thawing, Thermochim Acta 521 (2011) 184–190, https://doi.org/10.1016/j.tca.2011.04.022.
[41] M. Hirai, T. Hirai, T. Ueki, Growing process of scattering density fluctuation of a medium distance in the hydrogel of poly(vinyl alcohol) under stretching, Macromolecules 27 (1994) 1003–1006, https://doi.org/10.1021/ma00082a018.
[42] G. Beaucage, H.K. Kammler, S.E. Pratsinis, Particle size distributions from small-angle scattering using global scattering functions, J. Appl. Crystallogr. 37 (2004) 523–535, https://doi.org/10.1107/S0021889804008969.
[43] L. Huang, et al., Control nucleation for strong and tough crystalline hydrogels with high water content, Nat. Commun. 15 (2024) 7777, https://doi.org/10.1038/s41467-024-52264-y.
[44] N.A. Peppas, E.W. Merrill, Differential scanning calorimetry of crystallized PVA hydrogels, J. Appl. Polym. Sci. 20 (1976) 1457–1465, https://doi.org/10.1002/app.1976.070200604.
[45] J. Hao, R.A. Weiss, Mechanical behavior of hybrid hydrogels composed of a physical and a chemical network, Polymer 54 (2013) 2174–2182, https://doi.org/10.1016/j.polymer.2013.01.052.

[46] L. Xiong, et al., Network chain density and relaxation of in situ synthesized polyacrylamide/hectorite clay nanocomposite hydrogels with ultrahigh tensibility, Polymer 49 (2008) 5064–5071, https://doi.org/10.1016/j.polymer.2008.09.021.
[47] W. Fu, et al., Mechanical Properties and Mullins effect in Natural Rubber Reinforced by Grafted Carbon Black, Adv. Polym. Technol. 2019 (2019) 4523696, https://doi.org/10.1155/2019/4523696.
[48] J. Diani, B. Fayolle, P. Gilormini, A review on the Mullins effect, Eur. Polym. J. 45 (2009) 601–612, https://doi.org/10.1016/j.eurpolymj.2008.11.017.
[49] R.E. Webber, et al., Large strain hysteresis and Mullins effect of tough double-network hydrogels, Macromolecules 40 (2007) 2919–2927, https://doi.org/10.1021/ma062924y.
[50] R. Shi, et al., Elastic-plastic transformation of polyelectrolyte complex hydrogels from chitosan and sodium hyaluronate, Macromolecules 51 (2018) 8887–8898, https://doi.org/10.1021/acs.macromol.8b01658.
[51] J. Jia, et al., Salt-welding strategy for the design of repairable impact-resistant and wear-resistant hydrogels, Sci. Adv. 11 (2025) eadr9834. https://www.science.org/doi/10.1126/sciadv.adr9834.
[52] S. Huang, et al., Antifreezing hydrogel electrolyte with ternary hydrogen bonding for high-performance zinc-ion batteries, Adv. Mater. 34 (2022) 2110140, https://doi.org/10.1002/adma.202110140.
[53] Q. Guo, et al., Single proton anti-freezing hydrogel electrolyte with enhanced ion migration number enabling high-performance supercapacitor, Sustain. Mater. Technol. 41 (2024) e01066, https://doi.org/10.1016/j.susmat.2024.e01066.
[54] Y. Wang, et al., Lean-water hydrogel electrolyte for zinc ion batteries, Nat. Commun. 14 (2023) 3890, https://doi.org/10.1038/s41467-023-39555-5.
[55] N. Zhang, et al., Cation-deficient spinel $ZnMn_2O_4$ cathode in $Zn(CF_3SO_3)_2$ electrolyte for rechargeable aqueous Zn-ion battery, J. Am. Chem. Soc. 138 (2016) 12894–12901, https://doi.org/10.1021/jacs.6b05958.
[56] W. Sun, et al., A rechargeable zinc-air battery based on zinc peroxide chemistry, Science 371 (2021) 46–51, https://doi.org/10.1126/science.abb9554.
[57] S. Huang, et al., A self-healing integrated all-in-one zinc-ion battery, Angew. Chem. Int. Ed. 58 (2019) 4313–4317, https://doi.org/10.1002/anie.201814653.